Computing the radar cross section of dielectric targets using the Gaussian beam summation method

Mira Kaissar Abboud[1], Ali Khenchaf [1],* , **Philippe Pouliguen [2] and Thomas Bonnafont[1]**

1   Lab-STICC/SYPH/PIM, ENSTA Bretagne, 2 Rue François Verny, 29806 Brest
2   Agence de l'Innovation de Défense, 60 Bd du Général Martial Valin, 75509 Paris
*   Correspondence: ali.khenchaf@ensta-bretagne.fr;

Abstract: Computing the Radar Cross Section (RCS) of a given object is a topic of major importance for many applications, e.g. target detection and stealth technology. In this context, high-frequency asymptotic methods are widely used. In this article, we derive a Gaussian Beam Summation (GBS) method for both metallic and dielectric targets. The basic idea is to use the GBS method to compute the scattering far fields generated by the equivalent currents flowing on the surfaces. The validity of the proposed method is then investigated in the X-band. To accomplish this, the results obtained using this technique were compared to those obtained using other sufficiently accurate methods, such as the ray tracing of FEKO and the ray asymptotic solution. As an example of the method's accuracy, the GBS method was used to obtain the wave field in a homogeneous medium by fitting the results to a point source. In the same way, the method was used to compute the RCS of dielectric cuboids.

1. Introduction

In this paper, we are interested in computing the Radar Cross Section (RCS) of an electrically large object. As a matter of fact, modelling the electromagnetic wave scattering from a given object is a topic of major interest for many applications such as detection (e.g. radar [1,2]), for stealth technologies validation and optimization [3], or in inverse problems (e.g. inverse scattering [4]). This problem becomes quite challenging when the objects are electrically large. Indeed, rigorous methods, such as the Method of Moments (MoM) [5], are limited by their computational performances, since the mesh size needs to be of at least $\lambda/8$.

Therefore, high frequency asymptotic techniques, such as ray methods [6] or Physical Optics (PO) [7,8], have been extensively employed in order to find approximate solutions in a limited amount of time while keeping a good accuracy. In general, these latter come from an asymptotic evaluation of existing Green's functions for given conditions.

For example, Geometrical Optics (GO) [6,9] are based on the description of the field in terms of optical rays – plane waves – that follow Fermat's rule and are summed together at a given point to obtain the electric or magnetic field at this point. This latter is limited by the number of rays needed to accurately described complicated shapes and by the caustic phenomena. Another widely used asymptotic method is the PO one [7,8,10]. This technique corresponds to the asymptotic version of the MoM, where only the surface of the object is discretized and the radiation integral is computed over a set of equivalent currents on the surface. This computation is performed by assuming that the incident field is a plane wave, and that each facet is locally plane, leading to an easier calculation of the currents. For complex shape, shade areas needs to be determined in order to use the PO efficiently, thus GO is used. Nevertheless, both these methods compute accurate estimates of field

behaviour in the specular regions [11]. Additionally, they offer clear physical images that can be used to analyze how electromagnetic waves propagate in real-world contexts.

However, they do not take into account diffraction effects. As a consequence, some improvements have been proposed to overcome this problem, such as the Geometrical Theory of Diffraction (GTD) [12,13], the Uniform Theory of Diffraction (UTD) [14–16], or the Physical Theory of Diffraction (PTD) [17,18]. They consist in a theoretical extension of the GO (or PO) that provides a more comprehensive explanation of the mechanism of high-frequency wave propagation, i.e. diffraction and reflection, in order to correct the field computations outside the specular region. Nevertheless, the caustics problem persist and the computational efficiency decreases since more rays needs to be accounted for.

In the '80s, a new asymptotic method has been introduced where the field is described in terms of Gaussian beams, overcoming the caustic problem [19,20]. Indeed, the Helmholtz equation is reduced to the Parabolic Wave Equation (PWE) [21] and the solution is seeked in the form of a Gaussian beam. Since then, the method has been widely used to model the electromagnetic wave propagation [22–26] for diverse applications. In particular, in the context of RCS computation two main methods have been employed: the Gaussian Beam Summation (GBS) [27–30] and the Gaussian Beam Lauching (GBL) [23,25] techniques. The latter could be compared to the PO. The GBS works the same way as the GO but rays are replaced by Gaussian beams. Indeed, the incident wave is assumed to be a Gaussian beam, instead of a plane wave, but the overall principle remains the same.

The above methods use conventional methods to calculate the far scattering field generated by an electric current on a perfectly conducting surface. However, extensions are needed when dealing with dielectric targets and/or when dealing with a target on a dielectric ground (such as the sea). Usually, the scattering field for dielectric targets is generated by electric and magnetic equivalent currents, excited by the reflected electric and magnetic fields, and formulated using the Kirchhoff approximation [31,32] and the Fresnel coefficients.

In this paper, we are interested in extending the GBS approach to the RCS computation when dealing with large dielectric objects. To the author's knowledge, this extension, for the RCS computation, has not been dealt with before, since the GBS method has only been used to compute the RCS of perfectly metallic objects [27–29]. Therefore, we propose to use, in the same way as for the PO, the Fresnel reflection coefficient [33], in order to compute the scattered field from a dielectric material. Some numerical tests in the X-band, with comparison to the PO and FEKO, are proposed in order to validate the method. Besides, the influence of some parameters on the GBS accuracy is tested.

The remaining of the article is organized as follows. Section 2 comprises three subsections that outline the problem formulation, notations, and the step-by-step implementation of the GBS method. Initially, we present the 2D GBS method tailored for metallic scatterers, followed by its extension to incorporate dielectric targets. Furthermore, we detail the formulation of the 3D GBS method, enabling us to analyze scattering phenomena in a 3D space. Moving on to Section 3, we conduct a sensitivity analysis of the GBS method, examining its performance under different parameter settings. We then apply the GBS method to compute the RCS of metallic targets and compare our results with the results from FEKO and the PO theory. Additionally, we employ the GBS method to determine the RCS of a dielectric cuboid, offering insightful discussions on its characteristics. Lastly, Section 4 concludes the paper, discusses the method, and gives some perspective for future works.

2. Materials and Methods

In this section, we provide an overview of the problem formulation and introduce the notations used throughout the article to ensure clarity and consistency. We then delve into the GBS method, which is presented in three distinct parts. First, we explore the implementation and intricacies of the GBS method when applied to metallic scatterers in a two-dimensional setting. Next, we discuss the modifications and considerations necessary

to accurately compute the RCS of dielectric targets using the GBS method. Finally, we present the formulation of the three-dimensional GBS method, enabling the modeling and analysis of complex radar targets.

2.1. Formulation of the problem and notations

Let us begin by introducing the notations that are used in this article. The vectors and matrices are denoted in bold, such as $\boldsymbol{V}$ and $\mathbf{M}$. A unit vector is denoted with a hat such as $\hat{\boldsymbol{v}}$. The imaginary unit is denoted by j, and a $\exp(j\omega t)$ time dependence is assumed in this paper, with ω the angular frequency. The frequency is denoted by f, and k denotes the wave number. The computations are performed in a non-empty domain Ω, corresponding to free space. The usual notations $\boldsymbol{E}$ and $\boldsymbol{H}$ are used for the electric and magnetic fields, while $\boldsymbol{J}_e$, and $\boldsymbol{J}_m$ denote the electric and magnetic surface current density, respectively.

As mentioned in the introduction, we are interested in the computation of the RCS of a dielectric or metallic target, i.e. computing the scattered field when an incident field hits the object $\mathcal{O}$. This latter is assumed to be in the center of the domain. In this context, we are interested in obtaining the electrical field $\boldsymbol{E}$, so as to compute:

$$\sigma = \lim_{r \to \infty} 4\pi r^2 \frac{\|\boldsymbol{E}^{\mathrm{s}}\|^2}{\|\boldsymbol{E}^{\mathrm{i}}\|^2},\qquad(1)$$

where σ denotes the RCS, $\boldsymbol{E}^s$ and $\boldsymbol{E}^i$ the scattered and incident fields, respectively, and r the distance from the object. A schematic representation of the problem is given in Figure 1, where the target is plotted in red. The target is a dielectric object of relative permittivity $\varepsilon_r \in \mathbb{C}$, which is assumed to be constant in all $\mathcal{O}$.
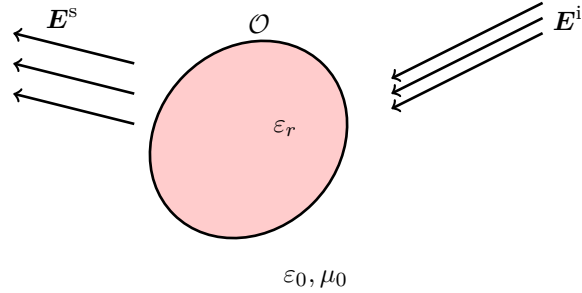

Figure 1. Schematic representation of the problem.

In this paper, we want to compute $\boldsymbol{E}^{\mathrm{s}}$ (and thus σ) at a given distance from the object r, with $r \gg \lambda$, with an object electrically large, i.e. its dimension D is such that $D \gg \lambda$. Thus, an asymptotic method is developed here to efficiently compute the RCS in these conditions. Indeed, with a rigorous method such as the MoM, the computations would be time-consuming and have a large memory footprint. The computations are performed both in 2D and 3D.

2.2. The Gaussian Beam Summation method

In this section the complete asymptotic computational scheme is developed. First, we recall the usual 2D GBS method when only a metallic object is accounted. Second, the method is extended to account for dielectric targets. Finally, the 3D formulation for the GBS method is explained.

2.2.1. The 2D GBS method for a 2D metallic scatterer

For better readability and understandability, the GBS method is recalled in 2D. The usual Cartesian coordinates (x, z) are used. In this context, the field can be decomposed in transverse electric (TE) and transverse magnetic (TM) components, with respect to the

z-axis. In both cases, either the field $\boldsymbol{E}$ or $\boldsymbol{H}$ have only one non zero components, i.e. E_y and H_y here. Therefore, we can study the scalar Helmholtz equation defined by:

$$\nabla^2\Psi(x,z,\omega) + k(\omega)^2\Psi(x,z,\omega) = 0, \tag{2}$$

with $\Psi = E_y$ or $\Psi = H_y$, and $\omega = 2\pi f$. This latter can be rewritten [19] as follows:

$$\nabla^2 u(x,z,w) + \frac{\omega^2}{c_0^2}u(x,z,w) = 0, \tag{3}$$

with c_0 the velocity of light at free space at a given point, and u the reduced field. Let Ψ and u be elements of the set Ω, where Ω corresponds to free space.

Then, a new coordinates system (s,n), i.e. the ray centred coordinate system, is introduced, in order to solve Equation (3). This latter is pictured in Figure 2. The idea of the GBS method is to search the solution u in terms of Gaussian beam [19,20]. One can think of them as a new basis for our field. Note that, s corresponds to the path length along the ray, while n corresponds to the path length perpendicular to the ray. Also, in (s,n) we denote by $v(s) = c_0$ the velocity along the ray. This latter simplifies the relations given in [19].
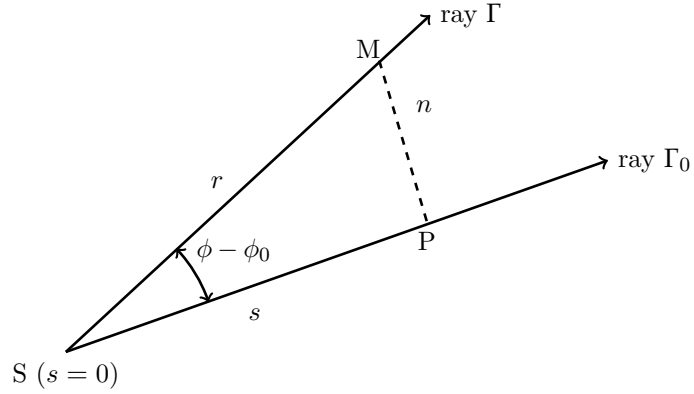

Figure 2. New ray centered coordinates system (s,n) around the ray Γ_0.

In this new coordinates, one can show [19,20] that the reduced field u can be obtained as:

$$u(s,n,\omega) = \left(\frac{c_0}{Q(s)}\right)^{1/2}\exp\left(j\omega\tau(s) + \frac{j\omega}{2}\frac{P(s)}{Q(s)}n^2\right), \tag{4}$$

where the ray-centered coordinate system around Γ_0 is provided. The central ray, denoted Γ_0, connects the computation point (where calculations or measurements are made) to the source (the origin or starting point of the rays). In this new system, any other ray such as Γ can be computed. In Equation (4), $\tau(s)$ is the travel time along the ray-path, and Q and P are solution of the following differential equation system:

$$\begin{aligned}\frac{dQ(s)}{ds} &= c_0 P(s) \quad \text{with} \quad Q(s_0) = \frac{-j\omega L_{\mathrm{M}}^2}{2c_0} \\ \frac{dP(s)}{ds} &= 0 \qquad\quad \text{with} \quad P(s_0) = \frac{1}{c_0}\end{aligned} \tag{5}$$

In this latter, P_0 and Q_0 correspond to the Hill's initial conditions [34], and L_{M} to the beam width at a given angular frequency ω. Both initial values of $P(s)$ and $Q(s)$ determine the width and the wavefront curvature of the Gaussian beams. A more thorough discussion on the choice of the parameter L_{M} is given in [19]. Note that the form of u of Equation (4) comes from the narrow-angle paraxial wave equation given in [19,20], assuming a Gaussian beam as the solution. Thus, the results are accurate in a paraxial cone of around $10°$

around the ray. Also, the define u corresponds to one given ray Γ. Besides, this solution is well-behaved when:

$$\mathrm{Im}\left(\frac{P(s)}{Q(s)}\right) > 0 \text{ and } |Q(s)| \neq 0 \,\forall s. \tag{6}$$

The optimal choice of the beam width L_{M} [19,20] depends on the frequency and on the distance along the ray from the initial point, and is given by:

$$L_{\mathrm{M}} = \left[\frac{2c_0}{\omega}(s - s_0)\right]^{1/2}, \tag{7}$$

where $s - s_0$ corresponds to the distance to the center of the object $\mathcal{O}$. In the following, we assume that the object is at the center of the domain leading to $s - s_0 = s$.

To compute the field at a given point M, we need to sum all contributions of the different Gaussian beams arriving at this point, as with the GO or PO methods. Using the linearity of the wave Equation (3), an approximate solution is given by the following expression:

$$u(M) = \int_0^{2\pi} \Phi(\phi) u_\phi(r, \phi, \phi_0) d\phi, \tag{8}$$

where ϕ_0 is the direction of the central ray toward M, r the distance of M from the object, u_ϕ corresponding to one contribution, and Φ corresponds to a weight function for each Gaussian beam. If this latter was known, then the integral could be directly computed. Therefore, a procedure to approximate it is described later on. Furthermore, to compute the integral we need to express each u_ϕ in the (r, ϕ) coordinate system.

Therefore, we begin by expressing u_ϕ in the polar coordinates system (r, ϕ). To do so, the differential Equation (5) needs to be solved leading to:

$$\begin{aligned} P(s) &= c_0^{-1} \\ Q(s) &= (s - s_0) + Q_0 \end{aligned} \tag{9}$$

Then, we express τ, s and n in the (r, ϕ) coordinate system as:

$$\begin{aligned} \tau(\phi, \phi_0) &= c_0^{-1} r \cos(\phi - \phi_0) \\ s(\phi, \phi_0) - s_0 &= r \cos(\phi - \phi_0) \\ n(\phi, \phi_0) &= r \sin(\phi - \phi_0) \end{aligned} \tag{10}$$

Finally, we obtain the following expression for u_ϕ:

$$u_\phi(r, \phi, \phi_0) = \left(\frac{c_0}{Q_0 + r\cos(\phi - \phi_0)}\right)^{1/2} \exp\left(-\omega\left[-\frac{j}{c_0} r\cos(\phi - \phi_0) - \frac{j}{2c_0}\frac{r^2 \sin^2(\phi - \phi_0)}{Q_0 + r\cos(\phi - \phi_0)}\right]\right), \tag{11}$$

where ϕ_0 corresponds to the take-off angle of the beam, and r the distance from the target.

Second, the function Φ is computed using the stationary phase theorem [35] as follows. Indeed, for a line source when $\omega \to \infty$, the Equation (8) must correspond to the exact solution of the wave equation, which is:

$$u_{\mathrm{ex}}(M) = -\frac{1}{4}\left(\frac{2c_0}{\pi\omega r}\right)^{1/2} \exp\left(j\frac{\omega r}{c_0} + j\frac{\pi}{4}\right). \tag{12}$$

Therefore, the expression of Φ is computed using the stationary phase theorem in order for $u(M)$ and $u_{\text{ex}}(M)$ to coincide. First, assuming a given r and ϕ_0, the two following functions are introduced:

$$
\begin{aligned}
F(\phi) &= \left(\frac{c_0}{Q_0 + r\cos(\phi - \phi_0)} \right)^{1/2} \\
f(\phi) &= -\frac{j}{c_0} r\cos(\phi - \phi_0) - \frac{j}{2c_0} \frac{r^2 \sin^2(\phi - \phi_0)}{Q_0 + r\cos(\phi - \phi_0)}.
\end{aligned}
\tag{13}
$$

Second, by deriving the function $f(\phi)$, the saddle point is obtained for $\phi = \phi_0$. Then, the second derivative of f is computed at $\phi = \phi_0$ leading to:

$$
\left[\frac{d^2 f(\phi)}{d\phi^2} \right]_{\phi=\phi_0} = \frac{jQ_0 r}{c_0(Q_0 + r)}.
\tag{14}
$$

The integral (8) is now approximated –steepest descent – as:

$$
u(M) = \Phi(\phi_0) c_0 \left(\frac{2\pi}{Q_0 \omega r} \right)^{(1/2)} \exp\left(j\frac{\omega r}{c_0} - j\frac{\pi}{4} \right).
\tag{15}
$$

Finally, by equalizing (15) and (12), we obtain:

$$
\Phi(\phi_0) = -\frac{j}{4\pi} \left(\frac{Q_0}{c_0} \right)^{1/2}.
\tag{16}
$$

Since Q_0 does not depend on Φ, we can conclude [36] that $\Phi(\phi)$ is a complex-valued constant and equals $\Phi(\phi_0)$ given by Equation (16).

The integral (8) can now be computed for any given ϕ_0 and r. For numerical reasons, the integral is discretized and computed as follows:

$$
u(M) = \sum_{k=1}^{N} \Phi_k u_{\phi,k} \Delta\phi,
\tag{17}
$$

with $\Delta\phi$ the angle step. Different discretization can be performed such as a simple trapezoidal one, or a more advanced like the Simpson one. Hence, for a given metallic target $\mathcal{O}$, the GBS method allows to compute its RCS. In the following section, the method is extended to account for dielectric target.

2.2.2. Extension of the GBS method for dielectric targets

In this section, the GBS method is formulated to account for a dielectric object. As mentioned in Section 2.1, $\mathcal{O}$ is assumed to be a dielectric material with constant ε_r in the coating. Since, as for the PO, we assume locally plane facets, each of them can be pictured as a plane surface, as plotted in Figure 3. The goal here is to derive, in the same way as for the PO method [33], an extension of the GBS for dielectric materials.
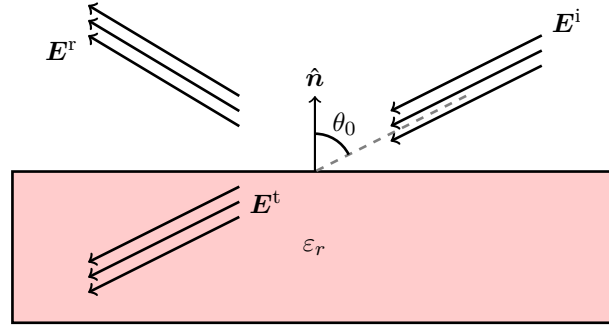
Figure 3. Schematic representation of the problem for a dielectric facet.

Here, we add the notation of $\boldsymbol{E}^t$ and $\boldsymbol{E}^r$ for the transmitted and reflected fields due to $\boldsymbol{E}_i$ striking the dielectric coating, and $\hat{\boldsymbol{n}}$ for the exterior normal. The computations are performed for a TE polarized electromagnetic wave, but calculations remain the same for the TM case. Besides, the size of the dielectric coating is $2b \times 2c$ along the horizontal and vertical dimensions. The angle of incidence from $\boldsymbol{E}^i$ on the object is denoted by θ_0.

On the surface of the dielectric, the following relation needs to be verified:

$$u^i = u^r + u^t. \tag{18}$$

Assuming that the 3 are Gaussian beams, we can rewrite them as follows:

$$
\begin{aligned}
u^i &= \Phi(\phi)^i \exp(\omega f^i(\phi)) \\
u^s &= \Phi(\phi)^s \exp(\omega f^s(\phi)) \\
u^r &= \Phi(\phi)^r \exp(\omega f^r(\phi))
\end{aligned}
\tag{19}
$$

Since (18) must be verify for $\omega \to \infty$, we have:

$$f^i(\phi) = f^r(\phi) = f^t(\phi), \tag{20}$$

as also shown in [22]. Therefore, only the weighting function Φ must be calculate again here. To do so, as for the PO extension for dielectric object [33], we will use the Fresnel coefficient. Note that this is equivalent to what is proposed for propagation applications with Gaussian frames in [24].

To obtain the appropriate Φ, as with a PEC, a solution is to calculate it by comparison with another asymptotic approach or analytic solution. Following this idea, let us assume that $\boldsymbol{E}^i$ is a plane wave striking the dielectric coating of depth $2c$. Thus, both the electric and magnetic fields are written as follows:

$$
\begin{aligned}
\boldsymbol{E}^i &= E_0 \hat{\boldsymbol{i}}_{\mathrm{i}} \exp\left(jk\hat{\boldsymbol{k}}_i \cdot \boldsymbol{r}'\right) \\
\boldsymbol{H}^i &= \frac{1}{\zeta_0} \hat{\boldsymbol{k}}_i \times \boldsymbol{E}^i,
\end{aligned}
\tag{21}
$$

with E_0 the wave amplitude, $\hat{\boldsymbol{i}}_{\mathrm{i}}$ the unit polarisation vector, $\hat{\boldsymbol{k}}_i$ the unit wave vector, $\boldsymbol{r}'$ the position vector, and ζ_0 the free-space impedance. Then, the reflected wave from the top surface of the target can be expressed using the reflection coefficient as:

$$
\begin{aligned}
\boldsymbol{E}^r &= \Gamma(\theta_0) E_0 \hat{\boldsymbol{i}}_{\mathrm{r}} \exp\left[-jk\left(\hat{\boldsymbol{k}}_{\mathrm{r}} \cdot \boldsymbol{r}' + 2c_0 \cos\theta_0\right)\right] \\
\boldsymbol{H}^r &= \frac{1}{\zeta_0} \hat{\boldsymbol{k}}_r \times \boldsymbol{E}^r,
\end{aligned}
\tag{22}
$$

where Γ corresponds to either the parallel or perpendicular Fresnel reflection coefficient. Thus, this latter can be computed for any given incident plane wave and dielectric material.

In this definition, we also have $\hat{\boldsymbol{i}}_{\text{r}}$ and $\hat{\boldsymbol{k}}_{\text{r}}$ the unit polarisation and wave vector for the reflected field. This latter can be obtained using the Snell-Descartes laws, with:

$$\hat{\boldsymbol{k}}_{\text{r}} = \hat{\boldsymbol{k}}_{\text{i}} - 2\hat{\boldsymbol{n}}(\hat{\boldsymbol{k}}_{\text{i}} \cdot \hat{\boldsymbol{n}}) \text{ and } \hat{\boldsymbol{i}}_{\text{r}} = \hat{\boldsymbol{i}}_{\text{i}}. \tag{23}$$

Finally, using the surface-equivalent principle [37], the scattered field in the exterior region, with r large, can be computed using the Stratton-Chu (or Trace) formula [31] considering the following equivalent surface electric and magnetic current densities:

$$\begin{aligned} \boldsymbol{J}_e &= \hat{\boldsymbol{n}} \times \boldsymbol{H}^r \\ \boldsymbol{J}_m &= \hat{\boldsymbol{n}} \times \boldsymbol{E}^r. \end{aligned} \tag{24}$$

After radiating the currents to obtain the desired field u_s, the function Φ is computed using the stationary phase theorem and approximating the integral (8) using the steepest descent method, as in Section 2.2.1. The RCS takes the simple form:

$$\sigma = \sigma_\infty |R_p|^2 \delta_{pq}, \tag{25}$$

where σ_∞ is the PO/GBS form for the backscatter cross section of the perfectly conducting target of the same shape and R_p is the reflection coefficient for an incident wave of polarization $p \in \{vv, hh\}$. The function δ_{pq} is the Kronecker delta. Now that the method has been completely explained in 2D, the extension to 3D is introduced.

2.2.3. Formulation of the 3D GBS method

In 3D, according to [38], the individual contribution of the beam is given by the equation:

$$u_\theta(s, n, \omega) = \left(\frac{ikQ_0}{8\pi^2} \right) \frac{1}{Q_0 + s} exp\left[ik\left(s + \frac{1}{2}\frac{n^2}{Q_0 + s} \right) \right] \tag{26}$$

where Q_0 is the arbitrary beam parameter [19,36] subject only to the constraint that $\text{Im } Q_0 < 0$. An exhaustive discussion of the dependence of the Gaussian beam summation method on Q_0 is provided in [22].

Second, the total field at a given point M corresponds to the sum of all Gaussian beams with different take-off angles θ arriving at M. This leads to the following integral:

$$u(M) = \int_0^{2\pi} \int_0^\pi \Phi(\theta) u_\theta(s, n, \omega) \sin(\theta) \mathrm{d}\theta \mathrm{d}\phi, \tag{27}$$

with u_θ the Gaussian beam defined by Equation (26) with a take-off angle θ and Φ the weighting function as in 2D. This integral can be simplified using the Fubini theorem, since from geometrical considerations, one can show that u_θ does not depend on ϕ [29]. Therefore, the integral is expressed as:

$$u(M) = \int_0^{2\pi} \mathrm{d}\phi \int_0^\pi \Phi(\theta) u_\theta(s, n, \omega) \sin(\theta) \mathrm{d}\theta. \tag{28}$$

To compute Φ, the same method as in Section 2.2.1 can be used, i.e. matching the integral with a well-known asymptotic result such as the ray theory or PO solution, as shown in [19,36]. Then, the integral is numerically computed as:

$$u(M) \simeq 2\pi \sum_{k=1}^N \Phi(\theta_k) u_{\theta_k} \sin(\theta_k) \Delta\theta, \tag{29}$$

using a discrete approximation of the integral, such as a Simpson rule [39], with $\Delta\theta$ the step along θ.

To account for a dielectric the same method as the one developed in Section 2.2.2 is used. Indeed, only the weighting function is changed by matching it to the scattered field

obtained by radiating the current densities of Equation (24), either analytically or with the PO asymptotic method. An example for a cuboid is given in Section 3 with a numerical test.

3. Results

In this part, some numerical tests are proposed to show the efficiency of our method. First, a sensitivity analysis of the GBS method over the different parameters of the Gaussian beam is proposed. Second, the method is used to compute the RCS of a PEC target. Finally, the method is used in the case of a dielectric object.

3.1. Sensitivity analysis of the GBS method with the parameters

In this section, we will study the impact of some parameters that affects the accuracy of the method:

- the wavelength λ,
- the distance r, between the receiver and the source (the object $\mathcal{O}$),
- the number of discreet angle to approximate the integral N,
- the half-beam width L_{M}.

We use the same test as in [36], with a comparison to the results provided by the point source [38] in order to validate the 3D GBS method and its implementation. Note that the field due to the ray asymptotic method is given by:

$$u_{\mathrm{G}} = \frac{\exp(j\omega r/c_0)}{4\pi r}. \tag{30}$$

We denote the amplitude of the GBS method and the ray asymptotic solution by A_{GBS} and A_{G}, respectively. The phases of the GBS and the ray asymptotic methods are denoted ϕ_{GBS} and ϕ_{G}, respectively. Note, that here, the angles are given in radians.

First, we test the effect of the wavelength on the accuracy of the method. The computations parameters are as follows: $r = 100$ cm, $\Delta\theta = 0.007$, $\theta_{\max} = 0.6981$, $N = 101$. Here the angle is measured in both directions from the central ray up to $\theta_{\max}$. Thus, the wave field is examined in a cone with an angle of $2\theta_{\max}$. For different λ, the results in terms of amplitude and phase are given in Table 1. Note that L_{M} is computed according to (7) for each value λ.

Table 1. Effect of the wavelength λ on the GBS results.

λ	L_{M}	A_{GBS}	A_{G}	ϕ_{GBS}	ϕ_{G}
0.62	4.4424	0.00079413	0.00079577	1.8231	1.8242
6.3	14.161	0.00079533	0.00079577	-0.78806	-0.79786
62.8	44.71	0.00074799	0.00079577	-2.2372	-2.5613

From Table 1, one can conclude that the GBS method is in perfect agreement with the the ray asymptotic method for different value of λ, even if a very large value of λ, i.e. a lower frequency f, the precision decrease, as expected.

We now test the method with different values of r. This latter increases from 100 cm to 500 cm. The parameters are as follows: $\lambda = 6.3$ cm, $\Delta\theta = 0.0087$, $N = 101$, $\theta_{\max} = 0.8727$. The optimal value of L_{M} is computed for each distance r. As before, the results are provided in Table 2.

Table 2. The effect of epicenter distance r on the GBS results.

r	L_{M}	A_{GBS}	A_{G}	ϕ_{GBS}	ϕ_{G}
100	14.161	0.00079524	0.00079577	-0.78817	-0.79786
200	20.0267	0.0003976	0.00039789	-1.5913	-1.5957
300	24.5277	0.000265	0.00026526	-2.3912	-2.3936
400	28.3221	0.00019869	0.00019894	3.093	3.0917
500	31.6651	0.0001589	0.00015915	2.2943	2.2939

As for the test on λ, we can conclude that the GBS method works well, and that the accuracy increases with r as expected. In the following test, the wavelength λ, the distance r and the step along θ is fixed in order to test the effect of the number of discrete angular points N. The test parameters are as follows: $\lambda = 6.3$ cm, $r = 100$ cm, $\Delta\theta = 0.005$, $L_{\mathrm{M}} = 14.161$. In this case, we have $A_{\mathrm{G}} = 0.00079577$, $\phi_{\mathrm{G}} = -0.79786$. The results in terms of amplitude and phase are given in Table 3.

Table 3. The effect of the width of the cone of rays on the GBS results.

N	ϕ_{max}	A_{GBS}	ϕ_{GBS}
121	0.6	0.00079546	-0.78797
101	0.5	0.00079577	-0.78761
81	0.4	0.0008022	-0.8005
61	0.3	0.0008483	-0.72034
41	0.2	0.00069109	-0.4339
21	0.1	0.00025856	-0.13658

As expected, with N, i.e. the density of rays, increasing, the accuracy of the GBS method increases [19]. Besides, when $N \geq 101$ the method is in perfect agreement with the one obtained with the complex point-source.

Finally, we show the effect of the effective half-beam width L_M, in particular when the optimal value is not used. The scenario parameters are: $\lambda = 6.3$ cm, $\Delta\theta = 0.0075$, $\theta_{\mathrm{max}} = 0.6$, $N = 81$. Note that in this case the optimal value of L_{M} would be 14.1. Besides, the point source leads to the following values for the amplitude and phase: $A_{\mathrm{G}} = 0.00079577$, $\phi_{\mathrm{G}} = -0.79786$. For the GBS, the results for different L_M are given in Table 4.

Table 4. The effect of the effective half width of the beam at the source on the GBS results.

L_{M}	A_{GBS}	ϕ_{GBS}
44.7	0.00077651	-1.0022
20	0.00079607	-0.79492
14.1	0.00079535	-0.78792
10	0.00079238	-0.75847
7.1	0.00076108	-0.66649
5.8	0.00070622	-0.58019

This test highlights that the optimal value of L_{M} is necessary to obtain a good agreement with the expected value.
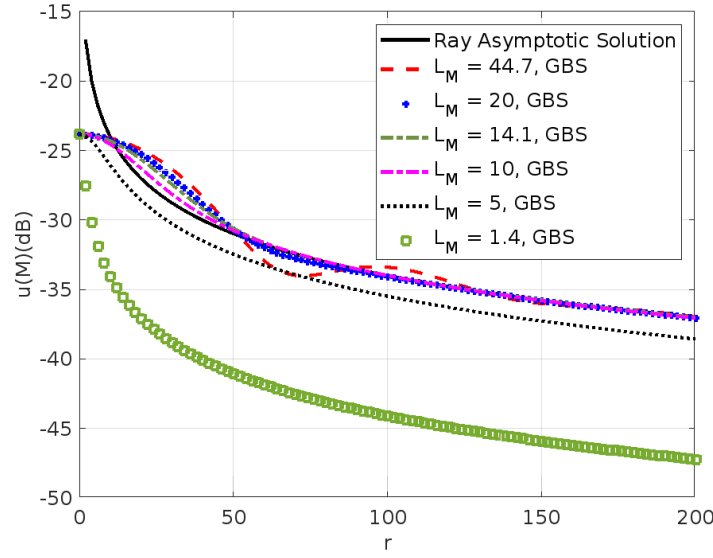
Figure 4. Variation of the amplitude of the field for different values of beam-width with a fixed number of beams N ($N = 81$).

Figure 4 compares the variation of the electric field obtained by the asymptotic ray theory and the Gaussian beam summation method as a function of the distance r. According to this figure, the results are in good agreement for $L_M = 10$, 14.1 and 20 when $r > 50$ cm. This confirms the conclusions of Tables 2 and 4.

In conclusion, this sensitivity analysis shows that, as expected and shown in [19], L_M must be computed using Equation (7), while we need to be further away from the source, i.e. r large, and a large frequency, i.e. a low λ. Besides, this shows that the GBS method works well, when good parameters are chosen. We can now use it to compute the RCS of different objects $\mathcal{O}$.

3.2. RCS computation of metallic targets using the GBS method

To illustrate the effectiveness of the proposed method, the mono-static RCS of two metallic targets as a function of θ have been computed and compared to other results. The investigated targets are a flat circular plate with radius $a = 7.5$ cm ($ka \approx 16$) and a flat circular plate with radius $a = 15$ cm ($ka \approx 31$). The results are shown in Figures 5 and 6. To validate the method, we compare it with the results of the PO and FEKO software, but also with experimental data acquired during measurements carried out in the anechoic chamber at ENSTA Bretagne.

The selection of computation parameters improves the correspondence between GBS results on the one hand and analytical results from PO, FEKO software, and measurements on the other. The results of the GBS method displayed in Figures 5 and 6 are obtained for $f = 10$ GHz, $r = 100$ and $N = 900$. The parameters Q_0 and L_M are defined in the Equation (5) and Equation (7), respectively.

Notice the peak at the normal incidence ($\theta = 0°$) and the decay that rapidly oscillates as a function of θ. With increasing ka, the radar cross section becomes more peaked at the normal incidence and oscillates faster, while decreasing ka results in a broadened peak and slower oscillations, but the shape remains unchanged in general. Regarding Figure 6, the peak of the measurement curve appears lower compared to the other generated curves. This discrepancy in peak amplitude could potentially be attributed to misalignment or deviation from the target's intended central position during the measurements.
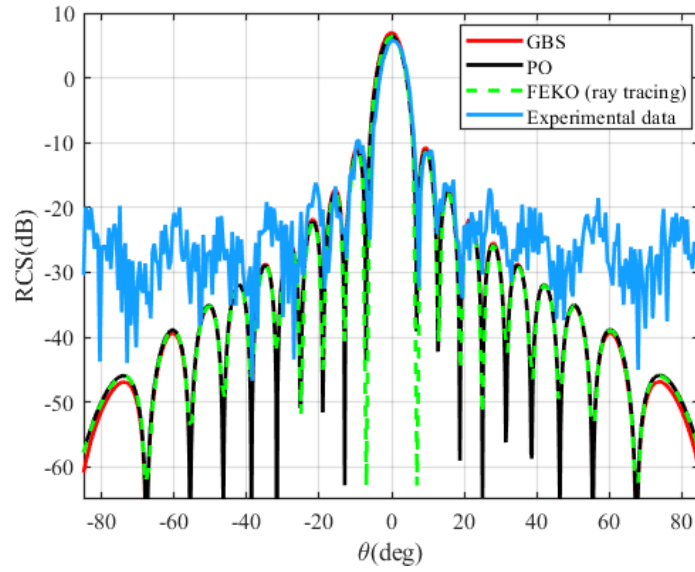
Figure 5. RCS at 10 GHz of a flat circular plate with a radius $a = 7.5$ cm (2a =5λ).
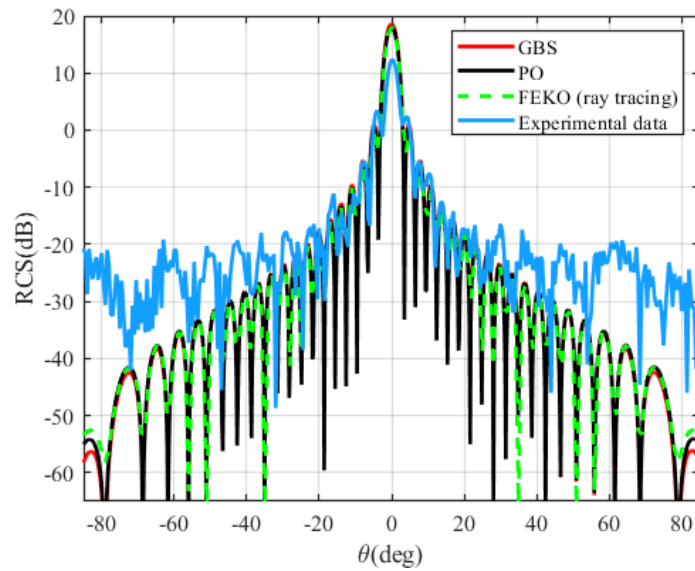

Figure 6. RCS at 10 GHz of a flat circular plate of radius a = 15 cm (2a=10λ).

3.3. RCS computation of a dielectric cuboid with the GBS method

In this section, the GBS method is used to compute the RCS of a cuboid of dimension $2a \times 2b \times 2c$, which corresponds to a dielectric material of permittivity ε_r. This latter is pictured in Figure 7. In this case, when a plane wave strikes the cuboid, one can analytically compute the electric field when the observation point is far from the target. Thus, the weighting function Φ is computed from this analytical result. Here, we assume a TE polarised plane wave as the incident field.
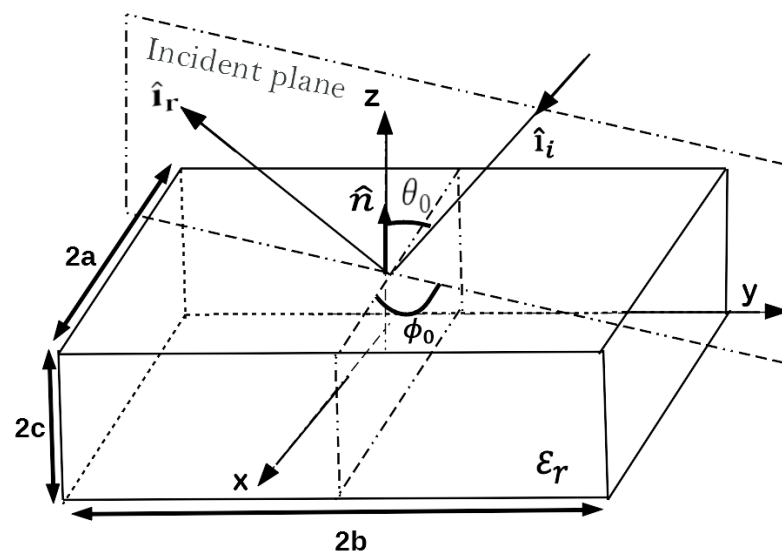
Figure 7. The geometry of the cuboid.
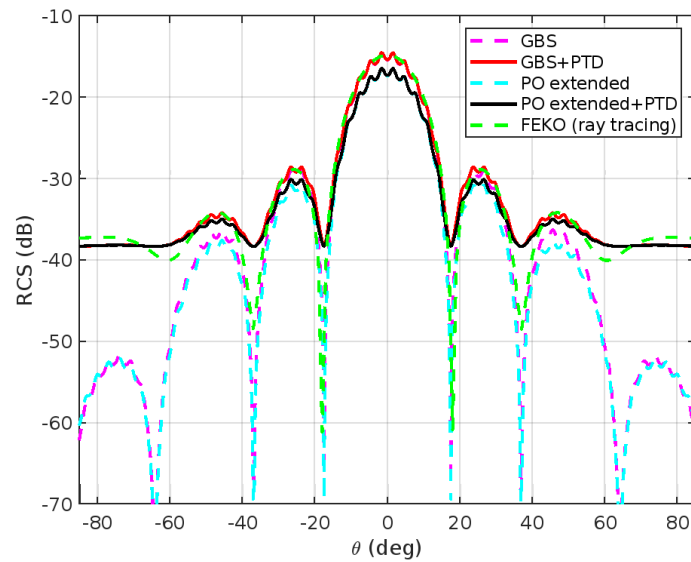
Figure 8. RCS at 10 GHz from the top surface of a thin cuboid, $\epsilon_r = 20 + 2j$; 2a = 2b = 5 cm $(2a = 2b = 1.6\lambda)$; 2c = 0.5 cm $(c = 0.16\lambda)$.
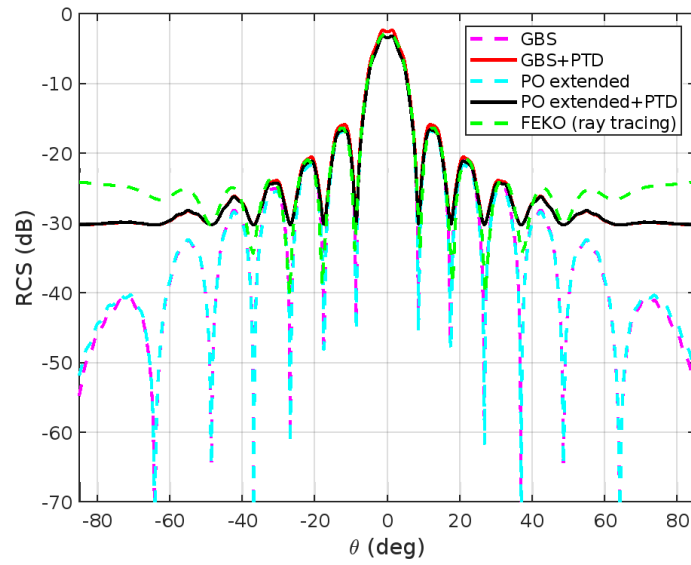
Figure 9. RCS at 10 GHz from the top surface of a thin cuboid, $\epsilon_r = 20 + 2j$; 2a = 2b =10 cm
$(2a = 2b = 3.33\lambda)$; 2c =1 cm $(2c = 0.33\lambda)$.

First, we use the GBS method to compute the scattered field (or the RCS) of two cuboids
of same dielectric parameters but different size. The first one is of size $2a = 2b = 5$ cm
and thickness $2c = 0.5$ cm, while the second one is of size $2a = 2b = 10$ cm and thickness
$2c = 1$ cm. Both are of the same material of permittivity $\varepsilon_r = 20 + 2j$. The results of
the computations performed with the GBS are compared to those of extended physical
optics [40,41] and the FEKO simulation in Figures 8 and 9. The computational parameters
are: $f = 10$ GHz, $r = 100$ cm and $N = 700$ for the Figure 8 and $N = 850$ for the Figure 9.

In both cases, the proposed method represents accurately the back-scattering phenom-
ena of large rectangular dielectric cuboids illuminated by a TE polarized plane wave. As
can be observed, our approach and the data derived using FEKO have a good agreement in
the specular reflection direction and areas nearby, as expected. The extended PO method
shows a slightly different result in Figure 8. For greater angles, both PO and our method
currently fail to account the diffraction caused by the two edges of the rectangular plate.

Nevertheless, these latter could be introduced using the PTD [17] for example. Included
in the Figures 8 and 9 are results based upon GBS and PO extended to which we have added
the fringe contributions from side edges thanks to the first order PTD approximation [42].
It can be seen, that the add of the fringe contributions provides a more accurate description
of the RCS close to the grazing angle ($\theta = 90°$). The graphs show that in Figure 8, the RCS
estimated with FEKO simulation and by the GBS and PO techniques, each combined with
the PTD, all converge to -38 dB at grazing angle. Examining the plots of the GBS and PO
techniques combined with PTD, respectively, in Figure 9 reveals that the RCS converges to
-30 dB at the grazing angle whereas the FEKO simulation converges to -24 dB.

Second, we test the sensitivity of the method to the dielectric permittivity. Therefore,
we study a dielectric cuboid of dimension $10 \times 10 \times 1$ cm^3 at $f = 10$ GHz. Since the GBS
method ignores edges near grazing angles, the fringe contributions are calculated using the
PTD approximation [42]. Only the real part of ε_r is changed along the first test. The results
obtained with the GBS method combined with PTD are compared with the commercial
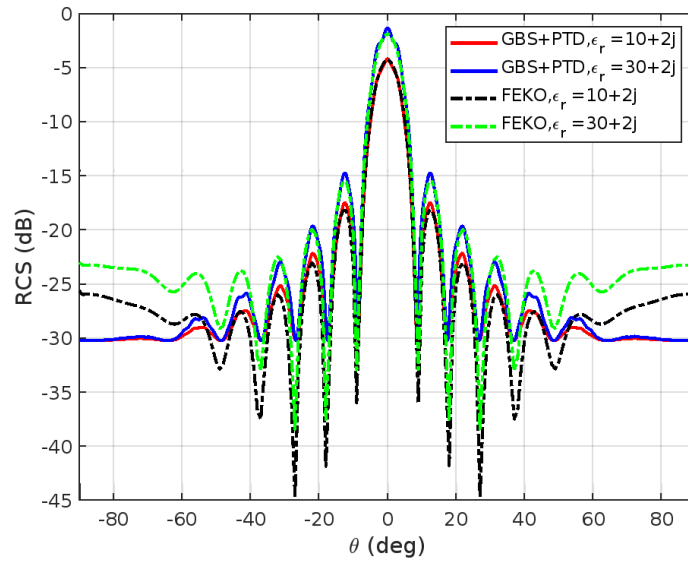FEKO software in Figure 10 for different ε_r.

Figure 10. RCS at 10 GHz from the top surface of a thin cuboid with various real part of permittivity and of dimension 2a = 2b =10 cm ($2a = 2b = 3.33\lambda$); 2c =1 cm ($2c = 0.33\lambda$).

As expected, with the real part of ε_r increasing, the RCS is increasing since the reflection coefficient increases. Besides, the results obtained with the GBS and FEKO are in good agreement, in particular in the specular region. Nevertheless, in our method, only the effect of simple diffraction is introduced yielding to slightly different results at the end of the domain of computations.

The following examples are used to test whether the RCS is affected by changing the imaginary part of the dielectric constant. Unless in exceptional circumstances, the behavior of σ as a function of θ remains as illustrated in Figures 8 and 9. Some examples of the radar cross section of two different cuboids with different lossy dielectric constants are shown in Figures 11 and 12 and compared to FEKO results. $\sigma(\theta)$ is shown for cuboids of size 15×15 cm^2, thickness $2c = 0.5$ cm and $2c = 15$ cm respectively at a frequency $f = 10$ GHz. Notice the tighter peak at normal incidence and the larger number of oscillations in comparison to Figure 10 which are due to higher ka. The computational parameters for GBS method are: $N = 900$ and $r = 100$.

The radar cross section can change drastically when the cuboid thickness becomes an odd multiple of half a wavelength. Figure 11 depicts σ in this case. For example, when the thickness is equal to $\lambda/6$ ($2c = 0.5$ cm) and the relative dielectric constant is $\epsilon_r = 10 + 0.5j$ (low loss), the waves at the cuboid's surface add up in phase and the reflection coefficient is very small. This is especially noticeable at normal incidence, where the peak amplitude is significantly reduced. If the dielectric has higher losses, the amplitude of the field changes as it passes through the cuboid, making this resonance less noticeable.

According to FEKO results in the Figure 12, a symmetric RCS pattern with respect to angle $\theta = 0°$ should be observed when the width and the thickness of the cuboid are identical. The results of the proposed method are different because of neglecting the effect of the others surfaces and the multiple diffraction.
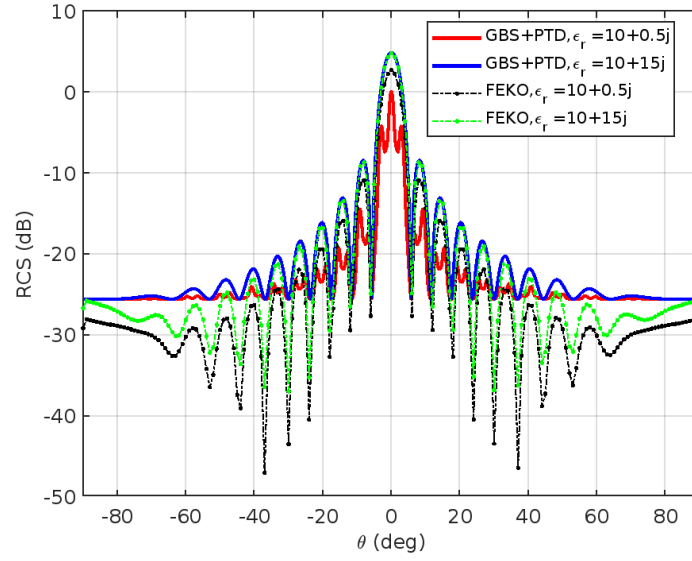
Figure 11. RCS at 10 GHz from the top surface of two different cuboids with various imaginary part of permittivity and of size $2a = 2b = 15$ cm ($2a = 2b = 5\lambda$); $2c = 0.5$ cm ($2c = 0.17\lambda$).
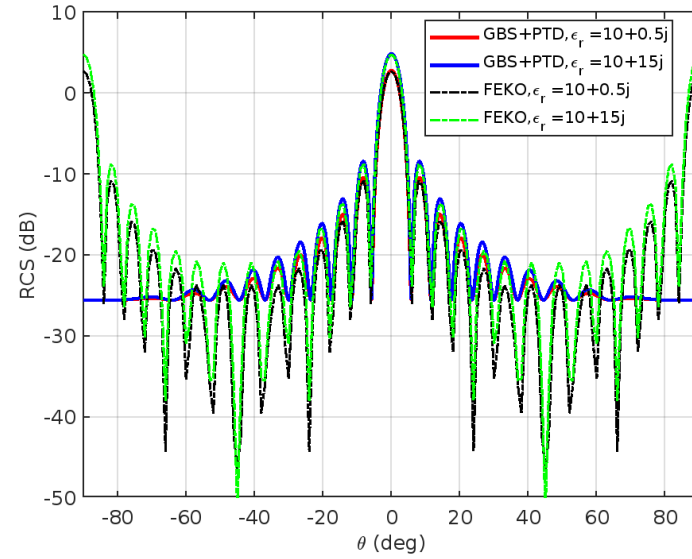

Figure 12. RCS at 10 GHz from the top surface of two different cuboids with various imaginary part of permittivity and of size $2a = 2b = 15$ cm ($2a = 2b = 5\lambda$); $2c = 10$ cm ($2c = 3.33\lambda$).

In conclusion, the solution given by the GBS approach applies for an arbitrary dielectric and an arbitrary thickness. Nonetheless, simulations for any shape and any angle of incidence can be implemented very effectively. However, the proposed method is by nature a high-frequency approximation and should therefore be applied with caution near the edges or when the minimum dimension of the dielectric target under study is not large compared to the wavelength. Even so, the limitations of the GBS method with respect to the scattered fields near grazing angles are mitigated by taking into account the first order of PTD contributions for the edges.

3.3.1. Trade-off between accuracy and computational cost

We now proceed to evaluate the efficiency of the method in terms of accuracy and computational time. As a starting point, we plotted the algorithm's execution time as a function of the number of calculation points. This analysis provides valuable insights into the computational efficiency and scalability of the method. Furthermore, we will calculate

the relative error to assess the accuracy of our method. Our focus will specifically be on
the specular direction, comparing it with the corresponding value obtained from FEKO.
This analysis will provide valuable information regarding the selection of computational
parameters, enabling us to strike a balance between the desired accuracy and the associated
computation time and memory requirements.

Figure 13 displays, on a logarithmic scale, the computation time of the GBS algorithm
as a function of the number of points N. The resulting curve exhibits a slope of 0.0018. This
relatively small slope reinforces the algorithm's effectiveness indicating that the increase in
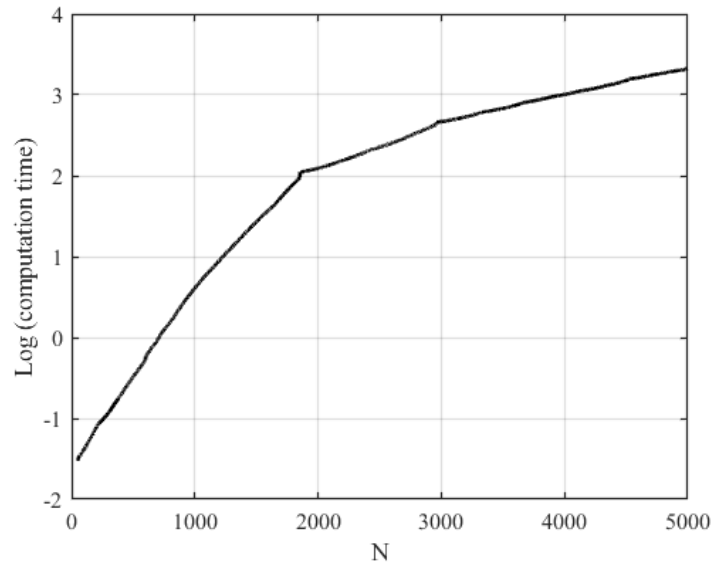computation time remains relatively low as the number of points increases.

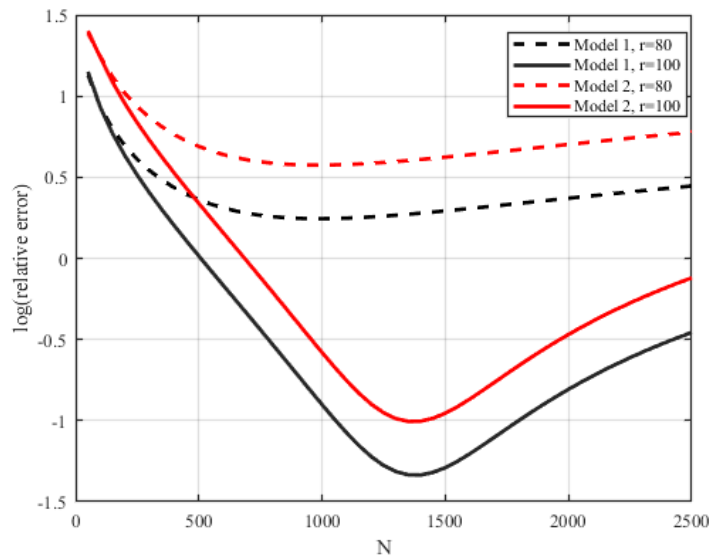**Figure 13.** Computation time vs. N.

Figure 14. Relative error vs. N.

To assess the algorithm's accuracy, we conducted a study involving two models of
different sizes. We specifically focused on rectangular targets, one with dimensions of
10×10 cm^2 (model 1) and the other with dimensions of 20×20 cm^2 (model 2), both
possessing a permittivity of 3.5. Our evaluation was based on calculating the relative error

between the specular direction obtained from the GBS method and the corresponding specular value provided by FEKO.

Our findings in Figure 14 revealed that as the size of the target increased, a greater number of points were necessary to achieve higher levels of accuracy. It was evident that increasing the number of points employed in the calculation generally led to improved precision. Additionally, it is worth noting that as the value of N increased, it was essential to correspondingly adjust the distance parameter, r.

By carefully analyzing the interplay between the number of points, target size, and distance parameter, we can effectively optimize the algorithm's accuracy across a diverse range of scenarios. This knowledge provides valuable insights into the necessary considerations for achieving desired levels of accuracy while employing the GBS method.

3.3.2. Exploring a different frequency range

In this study, we aim to broaden our understanding by examining the impact of a different frequency on the results of the GBS method. Throughout the article, we have exclusively focused on a frequency of 10 GHz. However, we recognize the importance of exploring the behavior and characteristics at a different frequency range. By testing an alternative frequency, we seek to gain insights into how the results adapt to a different frequency.

In this investigation, we have chosen the frequency of 6 GHz, which falls within the C-band range, to examine the RCS of a rectangular plate. The plate has dimensions of 20×20 cm^2, and its permittivity is set to 1.5. The computational parameters for GBS method are: N=1200 and r=120.

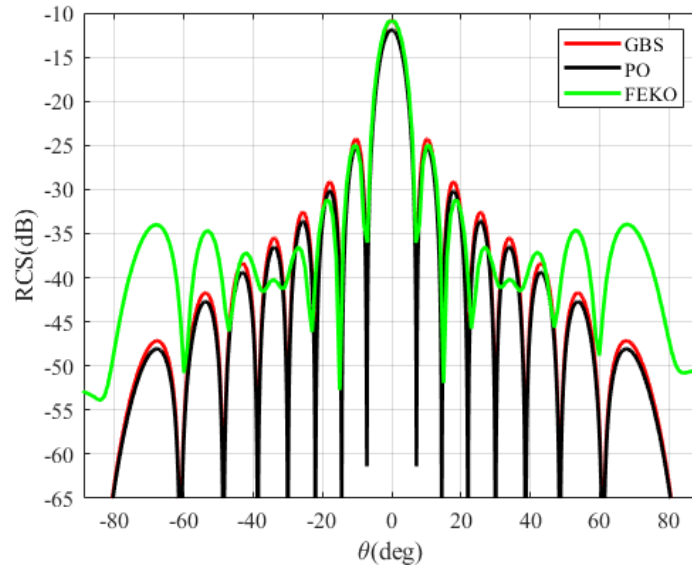**Figure 15.** RCS at 6 GHz of a dielectric rectangular plate of size $2a = 2b = 20$ cm ($2a = 2b = 4\lambda$).

Figure 15 illustrates a comparison between the results obtained using the GBS method, the PO approximation, and FEKO. The GBS result demonstrates a perfect agreement with FEKO within the angle range of -20 to 20 degrees. However, a slight difference becomes apparent as the angle increases beyond this range. This difference becomes more pronounced at higher angles of incidence ($> 50°$), indicating the presence of some divergences between the GBS and PO methods on the one hand, and the FEKO method on the other.

3.3.3. Application of GBS to realistic materials

The GBS method will be utilized to calculate the RCS of two different materials, namely FR4 and ABS. FR4 is a type of epoxy laminate reinforced with glass fibers that

is widely used in the production of electronics, specifically printed circuit boards (PCBs), due to its exceptional electrical properties and durability. Moreover, it is preferred in the aerospace industry because of its lightweight and high-strength features. The term "FR4" implies that it meets fire safety standards and stands for "Flame Retardant 4". FR4 can be tailored to fit specific design needs and is available in a variety of thicknesses. Its dielectric constant ranges from 3.9 to 4.6, depending on its composition and frequency, making it ideal for high-frequency applications such as PCBs and antennas [43].

In contrast, ABS is a thermoplastic polymer that is renowned for its durability, toughness, and resistance to impact and heat. It is frequently employed in the production of various consumer goods such as toys, electronic housing, and automotive parts. ABS also possesses excellent optical qualities, which makes it an ideal material for creating optical components like lenses [44]. ABS lenses find application in several domains, such as diffraction or focusing of light in optical systems. They are particularly useful in virtual and augmented reality applications, while focusing lenses are commonly utilized in cameras and projectors. The permittivity of ABS is dependent on its composition and frequency and typically ranges from 2.3 to 3.5, making it an excellent low-dielectric constant material for high-frequency applications. Hence, accurately characterizing the RCS values of both FR4 and ABS is essential for the optimization and design of radar systems in various sectors, including aerospace, defense, and telecommunications.

Furthermore, we propose to calculate the RCS of two identical targets with dimensions of $10 \times 10 \times 0.5$ cm^3 and permittivity values of $4 + 0.00075j$ for FR4 and $2.6 + 0.005j$ for ABS. It should be noted that the imaginary parts of the permittivity of the two materials in question correspond to common values. The calculations were performed at 10 GHz with $N = 900$ and $r = 100$.

Figure 16 illustrates a comparison between the RCS of ABS and RF4 using three different methods: GBS, PO, and FEKO. The curves representing the RCS of FR4 (represented by the dotted lines) are consistently above the curves representing the RCS of ABS (represented by the solid lines) over a wide range of angles for all three methods. This suggests that ABS is a more suitable material for stealth applications than FR4, and is likely to produce weaker radar echoes when illuminated by electromagnetic radiation. The differences in RCS between the two materials can be attributed to their different electromagnetic properties, such as permittivity. It is important to consider these differences when selecting materials for radar applications, as they can have a significant impact on system performance. Overall, the results of this comparison demonstrate the importance of accurate RCS calculations for understanding and optimizing radar systems.

A validation project is scheduled to confirm the accuracy of GBS method simulation results in characterizing dielectric materials like FR4 and ABS. The project involves carrying out RCS measurements in an anechoic chamber and comparing the obtained results with simulated values to ensure the accuracy and reliability of our method. This will expand options for future research and development.
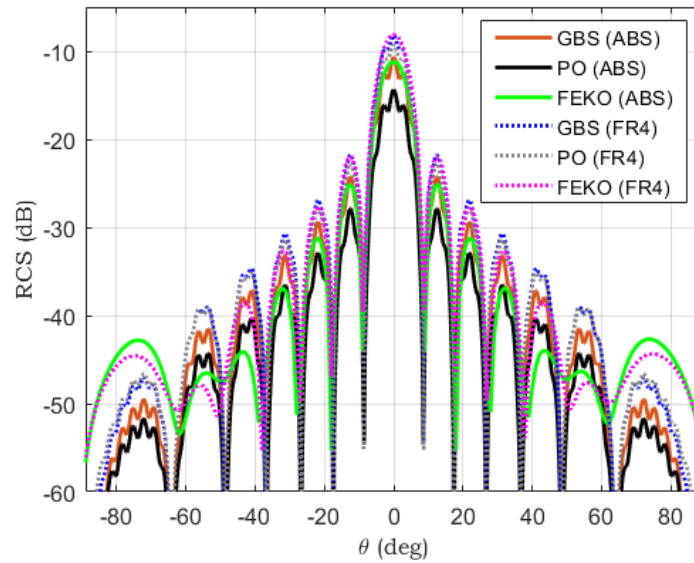
Figure 16. Comparison of RCS calculation for RF4 and ABS materials using GBS, PO, and FEKO.

4. Discussion and Conclusions

In this paper, the GBS method has been used in the context of radar applications and more particularly for the prediction of the scattering properties of a given target. The theoretical formulation of the Gaussian beam summation technique allows the calculation of the field in a homogeneous medium in three phases. In the first stage, a sufficiently dense ray tracing is performed from the source. Simultaneously to the first step, the calculation of the trajectories is performed step by step by solving the dynamic ray tracing system, numerically, with the appropriate initial conditions. This step consists in finding the coordinates of the observation point (neighboring ray) in the local reference frame and allows to determine the curvature of the wavefront and the amplitude profile of the Gaussian function. The third step is to sum all the contributions for the different rays, propagating in the vicinity of the main ray intercepting the receiver. For dielectric targets, we have thus formulated the integral solution, whose complex weighting function has been calculated by comparing the OP extended to the study of dielectric targets with that obtained by the fast descent path method. The assumed dielectric properties of the dielectric targets are taken into account by the Fresnel reflection coefficients which is contained in the weighting function Φ. This integral was discretized later for numerical solution.

The key benefit of this method is that it provides a very fast modeling methodology with excellent accuracy and efficiency for canonical targets. However, it can be extended to model a complex radar target by assembling a collection of relatively simple shapes, such as flat plates, cylinders, etc. The target's total RCS can be obtained as a coherent sum of the individual contributions.

Simulation results are presented to verify the efficiency and accuracy of the proposed method. The results are compared with those of FEKO using the ray tracing approach, and the extended formulation of the PO approximation for dielectric targets. The results show a good match in the specular direction. As the scattering direction moves farther away from the specular area, the physical optics and the Gaussian beam summation predictions fail by steadily wider margins.

The edge returns can be more accurately predicated in the non specular regions with PTD. This is because surface effects decrease to edge effect levels, and the edge contribution is not well modeled in PO and GBS. Indeed, induced currents are integrated over the illuminated parts of the body to obtain the far scattered fields. When applied to smooth bodies such as a flat plate, the PO generates an erroneous contribution due to the abrupt

discontinuity of the assumed surface fields at the shadow boundaries. The application of the first order PTD version of elementary edges waves which is free from the grazing singularity provides a significant improvement over large aspect angles in the estimation of the RCS. However, it is necessary to include multiple diffraction coefficients in order to account the multiple internal bouncing and the side surface effects when the thickness of the scattering targets is large. This aspect when the thickness increases will be pursuit in a future research.

In this paper we focus on the calculation of the RCS in the mono-static configuration of conductive and dielectric targets. The bi-static configuration will be the subject of another paper since the GBS formulation used allows easy switching from the mono-static to the bi-static configuration.

Author Contributions: Conceptualization, M.K.A. and T.B.; methodology, M.K.A., A.K., P.P and T.B.; validation, M.K.A., A.K. and P.P.; formal analysis, M.K.A. and T.B.; investigation, M.K.A. and T.B.; writing—original draft preparation, M.K.A.; writing—review and editing, T.B., A.K. and P.P.; supervision, A.K. and P.P.; project administration, A.K.; funding acquisition, A.K. and P.P. All authors have read and agreed to the published version of the manuscript.

Conflicts of Interest: The authors declare no conflict of interest.

Abbreviations

The following abbreviations are used in this manuscript:

RCS	Radar Cross Section
MoM	Method of Moments
PO	Physical Optics
GO	Geometrical Optics
PTD	Physical Theory of Diffraction
GBS	Gaussian Beam Summation
GBL	Gaussian Beam Launching
PEC	Perfect Electrical Conductor
PCB	Printed Circuit Boards
FR4	Flame Retardant 4
ABS	Acrylonitrile Butadiene Styrene

References

1. Burkholder, R.; Tokgoz, C.; Reddy, C.J.; Coburn, W.O. Iterative physical optics for radar scattering predictions. *ACES Journal* **2009**, *24*, 241–258.
2. Hwang, J.-T.; Hong, S.-Y.; Song, J.-H.; Kwon, H.-W. Radar Cross Section analysis using physical optics and its applications to marine targets. *J. appl. math. phys* **2015**, *3* 166—171.
3. Hamel, P.; Adam, J.P.; Kubické, G.; Pouliguen, P. Design of a stealth wind turbine. In Proceedings of the Loughborough Antennas & Propagation Conference (LAPC), Loughborough, UK, 2012.
4. Dorn, O.; Lesselier, D. Level set methods for inverse scattering. *Inverse Problems* **2006**, *22(4)* R67. doi:10.1088/0266-5611/22/4/R01
5. Gibson, W. C. *The method of moments in electromagnetics*; Chapman and Hall/CRC, 2021.
6. Deschamps, G. A. Ray techniques in electromagnetics. *Proceedings of the IEEE* **1972**, *60*, 1022–1035.
7. Nieto-Vesperinas, M. *Scattering and Diffraction in Physical Optics*, 2nd ed.; World Scientific Publishing, 2006.
8. Bennett, C. A. *Principles of physical optics*; John Wiley & Sons, 2022.
9. Luneburg, R. K. *Mathematical theory of optics*; Univ of California Press, 1966.
10. Harrington, R. F. *Time-harmonic electromagnetic fields*; IEEE Press, 2001.
11. Oodo, M.; Murasaki, T.; Ando, M. Errors of physical optics in shadow region-fictitious penetrating rays. *IEICE Trans. Electron.* **1994**, *77*, 995—1004.
12. Keller, J. B. A geometrical theory of diffraction. In *Calculus of Variations and Its Applications*; Proceedings of symposia in applied mathematics; McGraw-Hill, New York, 1958.
13. Levy, B. R. *Diffraction by a smooth object*; New York University, Graduate School, 1958.

14. Kouyoumjian, R. G.; Pathak, P. H. A uniform geometrical theory of diffraction for an edge in a perfectly conducting surface. *Proc. IEEE* **1974**, *62*, 1448–1461. doi: 10.1109/PROC.1974.9651.

15. Kouyoumjian, R. G.; Pathak, P. H.; Burnside, W. D. A uniform GTD for the diffraction by edges vertices and convex surfaces. In *Theoretical methods for determining the interaction of electromagnetic waves with structures*; Sijthoff and Noordhoff Netherlands, 1981; pp. 497—561.

16. Pathak, P. H. An asymptotic analysis of the scattering of plane waves by a smooth convex cylinder. *Radio Sci* **1979**, *14(3)*,419–435.

17. Ufimtsev,P. Ya. *Fundamentals of the physical theory of diffraction*; John Wiley & Sons, 2014.

18. Ufimtsev, P. Ya. Elementary edge waves and the physical theory of diffraction. *Electromagnetics* **1991**, *11(2)*,125–160.

19. Popov, M. M. A new method of computation of wave fields using Gaussian beams. *Wave motion* **1982**, *4(1)*, 85–97.

20. Cerveny, V. Gaussian beam synthetic seismograms. *J. Geophys.* **1985**, *58(1)*, 44–72.

21. Levy, M. *Parabolic equation methods for electromagnetic wave propagation*; IET, 2000.

22. White, B. S.; Norris, A.; Bayliss, A.; Burridge, R. Some remarks on the Gaussian beam summation method. *Geophys. J. Int.* **1987**, *89(2)*, 579–636.

23. Chou, H.-T.; Pathak, P. H.; Burkholder, R. J. Novel Gaussian beam method for the rapid analysis of large reflector antennas. *IEEE Trans. Antennas Propag.* **2001**, *49(6)*, 880–893. doi: 10.1109/8.931145.

24. Lugara, D.; Letrou, C.; Shlivinski, A.; Heyman, E.; Boag, A. Frame-based Gaussian beam summation method: theory and applications. *Radio Science* **2003**, *38(2)*.

25. Fluerasu, A.; Letrou, C. Gaussian beam launching for 3D physical modeling of propagation channels. *annals of telecommunications* **2009**, *64(11)*, 763–776.

26. L'Hour, C.-A.; Fabbro, V.; Chabory, A.; Sokoloff, J. 2-D propagation modeling in inhomogeneous refractive atmosphere based on gaussian beams part i: Propagation modeling. *IEEE Transactions on Antennas and Propagation* **2019**, *67(8)*, 5477–5486.

27. Leye, P.O.; Khenchaf, A.; Pouliguen, P. Gaussian beam summation method vs. gaussian beam launching in high-frequency rcs of complex radar targets. In 2016 IEEE International Geoscience and Remote Sensing Symposium (IGARSS), 2016; pp. 2630—2633.

28. Leye, P.O.; Khenchaf, A.; Pouliguen, P. RCS complex target, Gaussian beam summation method. In EUCAP 2016, 2016.

29. Leye, P.O.; Khenchaf, A.; Pouliguen, P. The Gaussian beam summation and the gaussian launching methods in scattering problem. *JEMAA* **2016**, *8(10)*, 219.

30. Leye, P.O.; Khenchaf, A.; Pouliguen, P. Gaussian beam summation method vs. Gaussian beam launching in high-frequency rcs of complex radar targets. In IEEE Conference on Antenna Measurments and Applications,(CAMA 2017), 2017.

31. Stratton, J.A.; Chu, L.J. Diffraction theory of electromagnetic waves. *Physical Review* **1939**, *56(1)*, 99.

32. Li-Xin, G.; Li-Cheng, J.; Zhen-Sen, W. Electromagnetic scattering from two-dimensional rough surface using the Kirchhoff approximation. *Chinese Physics Letters* **2001**, *18(2)*, 214.

33. Mohammadzadeh, H.; Nezhad, A.Z.; Firouzeh, Z.H. Modified Physical Optics approximation for RCS calculation of electrically large objects with coated dielectric. *Journal of Electrical and Computer Engineering Innovations (JECEI)* **2015**, *3(2)*, 115—1225. doi: 10.1109/APS.2013.6711606.

34. Hill, N.R. Gaussian beam migration. *Geophysics* **1990**, *55(11)*, 1416–1428.

35. Erdelyi, A. Asymptotic representations of Fourier integrals and the method of stationary phase. *Journal of the Society for Industrial and Applied Mathematics* **1955**, *3(1)*, 17—27.

36. Cerveny, V.; Popov, M.M.; Psencik, I. Computation of wave fields in inhomogeneous media - Gaussian beam approach. *J. R. Astron. Soc.* **1982**, *70(1)*, 109–128.

37. Schelkunoff, S.A. On diffraction and radiation of electromagnetic waves. *Physical Review* **1939**, *56(4)*, 308.

38. Norris, A.N. Complex point-source representation of real point sources and the Gaussian beam summation method. *JOSA A* **1986**, *3(12)*, 2005—2010.

39. A. Horwitz. A generalization of Simpson's rule. Approximation Theory and its Applications, 9(2):71–80, 1993.

40. Nguyen, A; Shirai, H. Electromagnetic scattering analysis from rectangular dielectric cuboids - TE polarization -. *IEICE Transactions on Electronics* **2016**, *E99.C*, 11–17.

41. Quang, H.N.; Shirai, H. High frequency plane wave scattering analysis from dielectric cuboids — TM polarization. In 2017 XXXIInd General Assembly and Scientific Symposium of the International Union of Radio Science (URSI GASS), pp. 1–4, 2017. doi: 10.23919/URSIGASS.2017.8105310.

42. Apaydin, G.; Hacivelioglu, F.; Sevgi, L.; Gordon, W.B.; Ufimtsev, P. Ya. Diffraction at a rectangular plate: First-order PTD approximation. *IEEE Transactions on Antennas and Propagation* **2016**, *64(5)*, 1891–1899. doi: 10.1109/TAP.2016.2536171.

43. Murugesan, A.; Natarajan, D.; Selvan, K. T. Low-Cost, Wideband Checkerboard Metasurfaces for Monostatic RCS Reduction. *IEEE Antennas and Wireless Propagation Letters*, **2021**, *20(4)*, pp. 493-497, doi: 10.1109/LAWP.2021.3054863.

44. Furlan, W. D.; Ferrando, V.; Monsoriu, J. A.; Zagrajek, P.; Czerwińska, E.; Szustakowski, M. 3D printed diffractive terahertz lenses. *Opt. Lett.* , **2016**, em 41(8), 1748-1751